Conf. 19

ANL/CP--74547

DE92 003414

Electron Energy Loss Spectroscopy in Advanced Materials

Nestor J. Zaluzec
Electron Microscopy Center for Materials Research
Argonne National Laboratory
Materials Science Division-212
Argonne, Illinois 60439

The submitted manuscript has been authored by a contractor of the U.S. Government under contract No. W-31-109-ENG-38. Accordingly, the U.S. Government retains a nonexclusive, royalty-free license to publish or reproduce the published form of this contribution, or allow others to do so, for U.S. Government purposes.

DISCLAIMER

This report was prepared as an account of work sponsored by an agency of the United States Government. Neither the United States Government nor any agency thereof, nor any of their employees, makes any warranty, express or implied, or assumes any legal liability or responsibility for the accuracy, completeness, or usefulness of any information, apparatus, product, or process disclosed, or represents that its use would not infringe privately owned rights. Reference herein to any specific commercial product, process, or service by trade name, trademark, manufacturer, or otherwise does not necessarily constitute or imply its endorsement, recommendation, or favoring by the United States Government or any agency thereof. The views and opinions of authors expressed herein do not necessarily state or reflect those of the United States Government or any agency thereof.

---

*Work supported by the U.S. Department of Energy, BES-Materials Sciences, under Contract No. W-31-109-Eng-38.

Invited Book Chapter for the Proceedings of TMS 1991 Annual Meeting & Exhibition, New Orleans, LA, February 17-21, 1991.

MASTER

DISTRIBUTION OF THIS DOCUMENT IS UNLIMITED

NOV 25 1991

Electron Energy Loss Spectroscopy in Advanced Materials

Nestor J. Zaluzec
Electron Microscopy Center for Materials Research
Argonne National Laboratory
Materials Science Division-212
Argonne, Illinois 60439

Abstract

The combination of a Transmission Electron Microscope (TEM) with an electron energy loss spectrometer (EELS) yields a powerful tool for the microcharacterization of materials. However, the application of this technique to advanced materials problems can only be fully appreciated when the information obtained using EELS is related to that obtained from other analytical spectroscopies. In this chapter, we briefly discuss the relative performance of X-ray, Auger and Photoelectron Spectroscopies with EELS pointing out the limitations and merits of each. This comparison is followed by examples of the application of EELS to investigations involving high T_c superconductors, artificial metallic superlattices, amorphous magnetic materials and the characterization of metallic hydride phases.

Table of Contents

Introduction....1
Relationship of Spectroscopies....2
Analytical Methodologies....3
Emission Spectroscopies....5
Absorption Spectroscopies....7
Comparison of Spectral Profiles
XEDS, XPS, EELS....7
XEDS versus EELS in the AEM
Practical Issues....10
Application of EELS to Materials Problems of Current Interest....14
Measurement of Valence Electron Densities
Studies of Hydrogen in Metals....15
Dielectric Function Measurements....19
Artificial Metallic Superlattices....22
High Tc Superconductors....23
Core Loss Spectroscopy....25
Valence Studies in Ti-based Ceramics....26
Amorphous Magnetic Materials....27
High Tc Superconductors....29
Summary....33
References....34
Index of Terms used in the Chapter....34

Electron Energy Loss Spectroscopy in Advanced Materials

Nestor J. Zaluzec
Electron Microscopy Center for Materials Research
Materials Science Division-212
Argonne National Laboratory

Introduction

The preceding chapters have covered transmission electron energy loss spectroscopy (EELS) from theory through instrumentation and application to studies in metals, minerals, ceramics, and semiconductors. In the chapters by Disko, Ahn, Leapman, and Rez the physics of the inelastic scattering processes and detailed descriptions of such parameters as the ionization cross-section, plasmons, dielectric functions, near edge and extended fine structure, and white lines, were thoroughly discussed. In this chapter we will touch briefly on these topics and apply them to studies of high Tc superconductors, multi-layer metallic superlattices, magnetic and amorphous materials and hydrogen in metals. In considering the application of EELS to technologically important or advanced materials problems whether they be practical applications or the investigations of newer materials such as High Tc superconductors it is essential to keep in mind the relationship of EELS to other analytical spectroscopies available to the experimentalist. Some of these spectroscopies such as characteristic x-ray, Auger, and photoelectron spectroscopy maybe preferred depending upon the questions being asked as they can yield complementary or more pertinent information. We will, therefore, begin this chapter by first briefly considering the relationship of the major analytical methods in use today. Of all the analytical spectroscopies, EELS in the TEM/STEM is most often used in conjunction with or opposed to XEDS and as a result we will spend some time discussing these two methodologies in order that the experimentalist can make an informed decision as to which technique is most appropriate for a given problem.

Relationship of Spectroscopies

Let us recall from chapter 1, that in EELS we are dealing with the coulomb interaction of an incident electron with either tightly bound inner shell

or the more loosely bound outer shell electrons of an atom in the solid. These atomic electrons are excited by the incident probe to a higher energy state in the solid or emitted from the surface as "secondary" electrons leaving behind a vacancy in the corresponding shell (figure1).

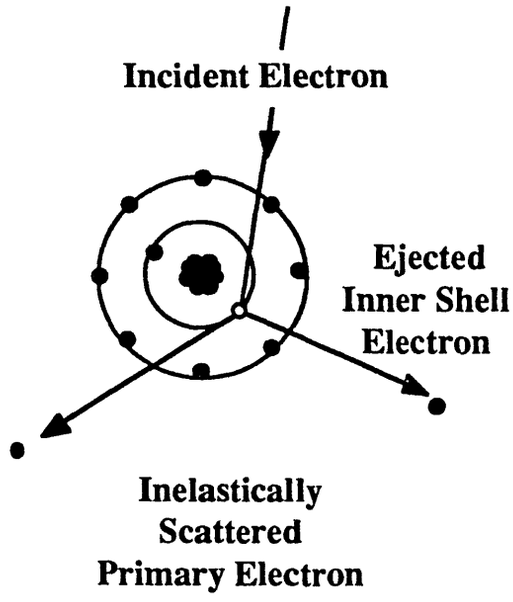

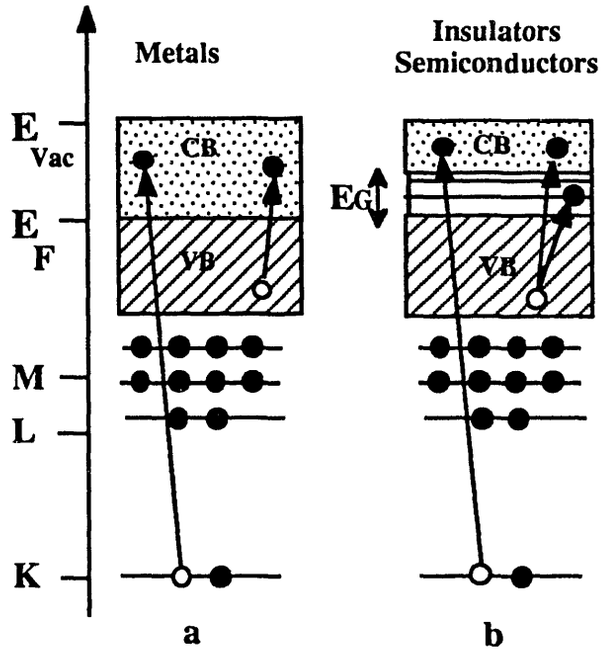

Figure 1. Basic Coulomb Interaction in EELS

Figure 2. Energy Level Diagram

These excitations are generally broken up into two regimes for ease of discussion. ***Core level*** excitations occur when the incident probe energy is sufficiently high to generate vacancies in the various inner shells (K = 1s, L=2s,2p.., M..) of the atom. Here, the ejected electrons are excited into the empty states above the Fermi level (figure 2a) and require an energy loss in the incident probe corresponding to the nominal binding energies of the respective levels (E_K,$E_{L,...}$). ***Valence band*** (VB) excitations require less energy and occur when the probe interacts with the outer shell electrons of the material. These excitations can occur in two manners. The first possibility is a single electron event similar to the inner shell case, where the ejected atomic electron is raised to an empty state in the ***Conduction Band*** (CB). In metals this can be to any of the continuum of states above the Fermi level (figure 2a), while in insulators or semiconductors the transition can also be to an empty interband state in the energy gap beyond the Fermi level (figure 2b). The second mode corresponds to a collective excitation of valence electrons in the solid as a whole. In quantum theory this is referred to as plasmon excitation and the energy loss corresponding to which is proportional to the local ***valence electron density*** of the material, this information can in turn be related to the dielectric constants

of the solid from which the optical properties can be derived. Subsequent to either the inner or outer shell excitations the atoms of the material are left in an excited or higher energy state. The process by which the atoms in the material return to their ground state by filling the energy level "holes" releases this excess energy. This can be in the form of heat (phonons), measurable photons (light and/or x-rays), or electrons (secondary, auger....) all of which can be used for further characterization of the specimen. The steps in this excitation/relaxation process are: 1.) excitation of the atomic electron to a higher energy level or complete ejection from the atom and the creation of a corresponding vacancy, 2.) filling of the vacancy by transition of an atomic electron from a higher energy level down, 3.) the emission of a electron (figure 3a,b) or photon (figure 3c) to achieve energy balance. The energy and intensity of the emitted particles and/or photons as well as loss in the same of the excitation source are the measurable quantities which are used to characterize a material and forms the basis of many other analytical spectroscopies.

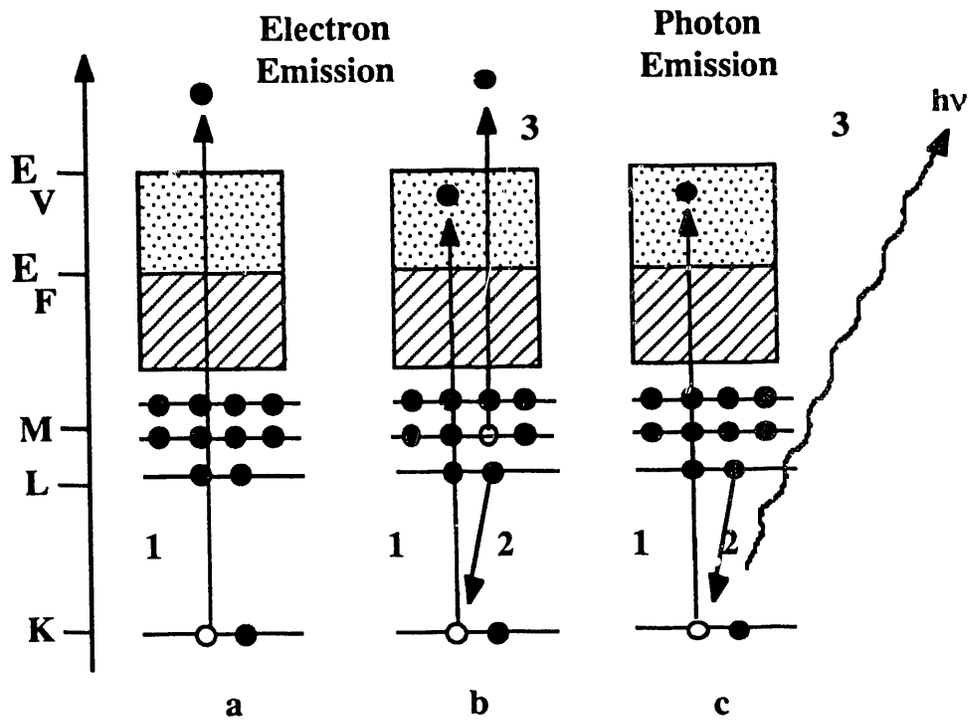

Figure 3. Steps in the emission process: 1-Excitation, 2-Relaxation, 3-Emission

Analytical Methodologies

Although the thrust of this book deals with primary excitation arising from incident electrons, a multitude of analytical methodologies have been developed over the years which also employ photons to achieve the effects just discussed. Thus we can consider in this scheme, four possible combinations of

source/emission signals: Electron-Electron, Electron-Photon, Photon-Electron, and Photon-Photon. Today this represents at least 14 major methodologies which include:

Table 1

Major Analytical Methodologies used in Materials Characterization

Electron-Electron	•Electron Energy Loss Spectroscopy (EELS), EXtended Energy Loss Fine Structure (EXELFS), Energy Loss Near Edge Fine Structure (ELNES), •Auger Electron Spectroscopy (AES),
Electron-Photon	•X-ray Emission Spectroscopy (XES), X-ray Energy Dispersive Spectroscopy (XEDS), Wavelength Dispersive Spectroscopy (WDS), •Cathodoluminescence (CL),
Photon-Electron	•X-ray Photoelectron Spectroscopy (XPS), X-ray Photoelectron Microscopy (XPM), •Ultraviolet Photoelectron Spectroscopy (UPS),
Photon-Photon	•X-ray Absorption Spectroscopy (XAS), EXtended X-ray Absorption Fine Structure (EXAFS), X-ray Absorption Near Edge Fine Structure (XANES) •X-Ray Fluorescence (XRF).

For brevity, we have not included the related techniques based upon the use of Ion Beams as either the excitation source or measured emission signal. It should also be pointed out that some of these methods can be configured with multiple detection schemes. For example, XANES experiments can be arranged to monitor both emitted photons as well as electrons.

In general, those methods using electrons as the excitation source have the higher lateral spatial resolution that those based upon photons, simply due to the fact, today, the intense nanometer diameter electron probes can be more readily produced than their photon counterparts. Listed in Table 2 are estimates of the best resolution of each technique (i.e assuming that one is using the perfect specimen!) and for comparison, the lateral resolutions some of the major elastic scattering techniques. The major thrusts of these elastic scattering methods are in atomic location determination, rather than spectroscopy, as they

deal with interactions of the incident probe with the nucleus instead of the outer electrons.

Technique/	Resolution	Technique/	Resolution	Technique/	Resolution
Electron-Electron		**Photon-Electron**		**Electron Scattering**	
EELS - Thin Film	~ 1 nm	AES - Bulk	~100 µm	TEM - Thin Film	~ 0.1 nm
- Bulk	~ 10 µm			STEM - Thin Film	~ 0.2 nm
EXELFS- Thin Film	~ 1 nm	XPM - Bulk	~ 1 µm	TED - Thin Film	~ 10 nm
ELNES - Thin Film	~ 1 nm	XPS - Bulk	~ 10 µm		
		UPS - Bulk	~1000 µm	SEM - Bulk	~ 1 nm
AES - Thin Film	~ 5 nm			ECP - Bulk	~ 10 µm
- Bulk	~ 50 nm	EXAFS - Bulk	~ 100 µm		
		XANES - Bulk	~ 100 µm	RHEED-Bulk	~100 µm
				LEED - Bulk	~100 µm
Electron-Photon		**Photon-Photon**		**Other Scattering**	
XEDS - Thin Film	~ 5 nm	XAS - Bulk	~ 100 µm	XRD - Bulk	~100 µm
- Bulk	~ 1 µm	EXAFS - Bulk	~ 100 µm		
WDS - Bulk	~ 1 µm	XANES - Bulk	~ 100 µm	ND - Bulk	~1000 µm
CL - Bulk	~ 1 µm	XRF - Bulk	~ 100 µm		

Table 2. Comparison of Some Major Inelastic/Elastic Scattering Techniques in Materials Science. Following each method is the principle specimen geometry, and estimated best lateral spatial resolution for an ideal specimen/system.

The Emission Spectroscopies UPS, XPS, XEDS, CL, AES, and XRF rely upon the measurement of a secondary signals generated subsequent to the primary excitation event. Their characteristic signatures are derived from the difference in initial and final energy states of the respective electronic transitions involved.

XPS and UPS employ X-ray and Ultraviolet radiation, respectively, to excite core level or valence shell electrons beyond E_{vac} for eventual measurement (figure 3a). The energy of the emitted electron is equal to the incident photon energy minus the kinetic energy of the ejected photoelectron (i.e. its binding energy). Thus, both these spectroscopies map out the ***occupied density of states below the Fermi level*** of their originating shells. Since low energy x-rays (< 2 keV) or UV photons are used as the excitation sources, these techniques probe the outer electron shells and are thus extremely sensitive to both the chemical and electronic structure of a material. The X-ray Photoelectron Microscope (XPM) uses a wide x-ray beam to irradiate large areas of a specimen. The subsequent photoelectron emission from the specimen is spatially focussed and energy filtered by electromagnetic and/or electrostatic lenses onto a two dimensional imaging detector system. This yields substantially increased lateral spatial resolution relative to conventional microfocus XPS systems which rely only on collimated photon probes. Since the primary energy is low, the emitted

photoelectrons in XPS and UPS are correspondingly low in energy. This low energy has the consequence that the photoelectrons have an extremely short escape depth of tens to hundreds of Angstroms and both methods tend to be classified as a surface sensitive/analysis techniques.

After the initial excitation event, whether by electron or photon beam, each atom must release its excess energy. During the relaxation back into a ground state a competition between the mechanism of energy release determines the processes which occur next and which signal will be emitted by the solid. For light elements electron emission dominates (the Auger effect), while for higher atomic number materials x-ray photons are more prevalent. The transition between these modes is gradual and perfectly complementary. For $Z<20$ in excess of 90% of the emission is by Auger emission while for $Z>60$ over 90% is x-ray photon emission, the 50% level occurs at about atomic number 35. In Auger spectroscopy, the emitted electrons result from multiple transitions (figure 3b) and the energy of the emitted electron (E) is characterized by three electronic subshells ($E = E_1-E_2-E_3$). E_1 is the initially ionized shell (#1-fig 3b), E_2 the shell which contributes its electron to fill the vacancy in E_1 (#2-fig 3b) and E_3 the shell emitting the detected electron (#3-fig 3b). Density of states information is present in AES data, however, due to the multiple shell processes involved it is more complex to interpret, thus AES is primarily used in elemental and chemical analyses. Due to the low energies involved in the Auger electron emission is also a surface sensitive technique.

In XEDS, CL and XRF, photon emission corresponds to the energy difference (E_1-E_2) between the initial and final states occurring during the atomic relaxation step (#2 of figure 3c) when the higher level electron drops down to fill the vacancy created by the primary excitation. These levels are generally well defined and discrete, corresponding to deep core losses resulting in characteristic emission lines in both XEDS and XRF. The information derived is, therefore, mainly representative of the atomic elements which are present, rather than the nuances of the bonding/electronic structure. These methods are most frequently used in quantitative compositional measurements and generally involve the emission of higher energy (~1-40 kV) photons. Due to their high energy, the integrated signal can be detected from deep within the material and XEDS and XRF are generally considered bulk analysis techniques having lateral spatial resolutions on the order of microns. An exception occurs when a "thin film" specimen is used and in this case, the spatial resolution is limited only by the scattering within the specimen thickness. For application in an AEM lateral resolutions $\leq$ 5 nm can be obtained. In Cathodoluminescence the transitions

giving rise to the emitted signal are between impurity states in the band gap of a material. Due to the smaller energies involved this gives rise to visible light and is most often applied to minerals or the study of defect states in semiconductors.

The Absorption Spectroscopies: EELS, EXELFS, ELNES, XAS, EXAFS, and XANES generally employ nearly monochromatic probes to irradiate a material. Their characteristic signatures are derived from the excitation of discrete inner shell levels into states above the Fermi level (figure 3 b & c). Conservation of energy requires that the excitation source loose a corresponding amount of energy and intensity and these are the parameters recorded in an experiment. The relative energy and intensity distribution, therefore, maps out the ***empty density of states above the Fermi level*** of the material being studied scaled by the probability that the particular transition will occur.

In the transmission x-ray methods (XAS, EXAFS, XANES) a fixed energy photon beam is incident upon the specimen and integrated attenuated signal is then monitored at each energy. The photon beam energy is then incremented and the process repeated building up a spectrum sequentially. The attenuation is a logarithmic function of the form $I_T=I_0\exp(-\mu t)$, with I_T and I_0 being the transmitted and incident intensities and t the relative thickness. The parameter of interest is generally μ the linear absorption coefficient as a function of energy. For the most part XAS and its associated methods (EXAFS, XANES) tend to deal with high energy absorption events greater than ~ 2 keV, however recent development of the high brightness synchrotron sources have extended the application of these spectroscopies to the lower energy absorption regime. Careful experiments have been conducted down as low as ~400 eV. In the electron transmission counterpart to XAS, namely EELS, we fix the incident energy and intensity and measure the transmitted intensity distribution at fixed energies using either serial or parallel detector systems. EELS as discussed in Chapters 1-4, is most powerful in the energy loss regime up to ~ 2 keV, although work as high as 10 keV has been reported.

Comparision of Spectral Profiles: XEDS, XPS, EELS

In order to appreciate the relative merits of both emission and absorption spectroscopies, partial spectral profiles representative of these methods are collected in figure 4. The data shown are all recorded from nominally pure copper, and is representative of XEDS (or XRF), XPS (or AES), and EELS (or XAS).

In figure 5, a schematic density of states for copper is sketched, which we

can use to explain the details of these experimental spectra. To begin, consider first the XEDS spectrum. The nearly Gaussian shaped peak of at the top of figure 4 signal here is derived from the L shell x-ray photon emission and is the result of discrete M_4->L_3 and M_5->L_3 transitions and hence only single emission lines ($L_{\alpha 1}$ and $L_{\beta 1}$) are allowed. The broad peak reflects the poor energy resolution typical of the energy dispersive solid state detector system (~100 eV) used to measure the Cu $L\alpha$, $L\beta$ signal rather than the intrinsic width of the x-ray lines in question (typically a few volts wide).

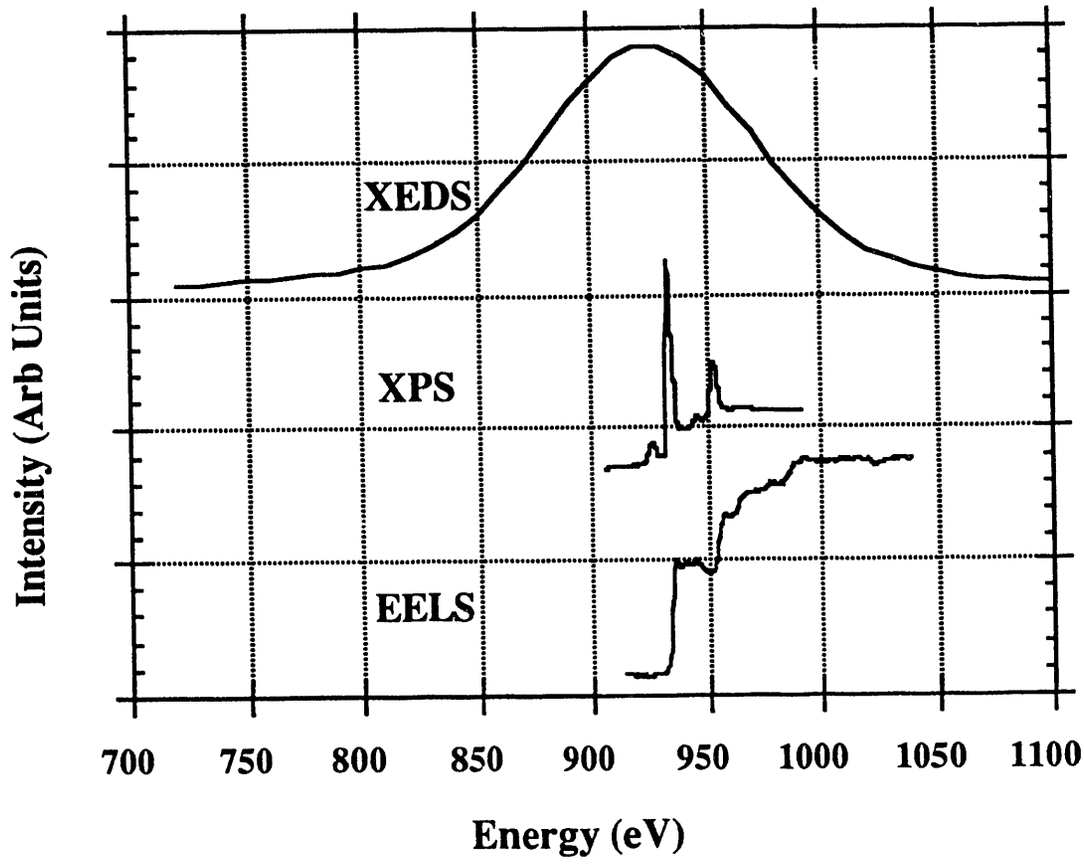

Figure 4. Experimental XEDS, XPS, and EELS data from the Copper L shell. Note the differences in energy resolution, and spectral features.

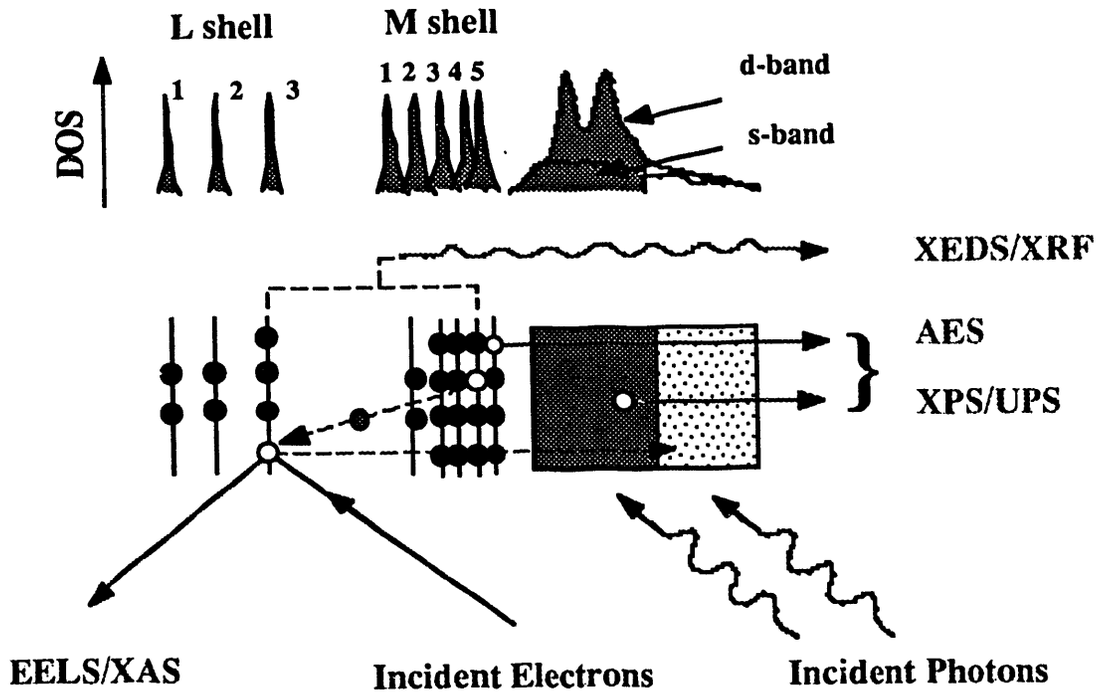

Figure 5. Schematic Diagram illustrating sources of XPS, AES, XEDS, and EELS signals detected from Copper. See experimental data in figure 4.

Wavelength dispersive spectroscopy would yield better energy resolution (~10-20 eV) but is less frequently employed today as the solid state detectors are so much simpler to use. At the center of figure 4 is the corresponding XPS L Shell electron emission spectrum derived from the ejection from $2p^{1/2}$ and $2p^{3/2}$ shells into vacuum and in contrast to the XEDS data shows a wealth of structure corresponding to the electronic structure of the d-band of copper. In metallic copper, the electronic structure is $3d^{10}4s^{1}$ and hence the d-band is fully populated. This means that maxima in the density of states must lie just below the Fermi level and are fully occupied. By comparison with figure 4b, one can see an excellent correspondence with intensity peaks observed in the experimental Cu XPS data sets. Since the d-band is full the density of states above the Fermi level must be correspondingly low. This implies that absorption transitions such as those typical of EELS (or XAS) which probe the related excitations 2p->3d are essentially forbidden, and only the weaker 2p->4s transitions can contribute to the edge profiles. This is clearly reflected in the EELS profiles as the onset of each edge, although sharp, levels off quickly with only small subsidiary oscillations above background.

Other materials will exhibit spectra which lie between these extremes. For example, nickel has intensity maxima in both XPS and EELS profiles since there are both occupied as well as unoccupied electronic states above and below the

Fermi level which are probed by both methods. In addition, as we shall see by way of example later in this chapter, alloying additions shift the Fermi level and can radically change spectra and provide valuable information about the electronic state of the material.

XEDS versus EELS in the AEM: Practical Issues

In many analytical electron microscope laboratories today, one is likely to find the capabilities for both XEDS and EELS. The novice rightly should ask "Which should I use for analysis?" A few years ago, if the experimentalist was interested in light element (Z<11) analysis in the AEM the only method available would have been EELS and this was generally the major motivation for acquiring EELS systems. The basic reason for this was instrumental. XEDS detector construction typically involves using a thin ~8-15 μm thick Beryllium window for environmental isolation to protect the LN_2 cooled Si(Li) detector. This window severely absorbs all photons below ~ 1 keV [Zaluzec et al. 1984]. Recently, commercial manufacturers have developed x-ray detector systems employing Ultra-Thin Windows (UTW) or Windowless (WL) configurations for the AEM. These new detector systems now permit acquisition of elemental spectra routinely through C, N, and O and in some models can extend detection capabilities downward in atomic number to Boron [Zaluzec,1990]. The differences in spectra obtained in these configurations (Be vs. Windowless/Ultra-Thin windows) in the energy range below 1 keV are remarkable. Figure 6 shows a comparison for NiO using Be and WL systems recorded in an AEM. Detection efficiency at the Ni L (0.85 keV) has increase nearly 5 fold, while the previously undetected Oxygen peak (0.53 keV) is now readily measured.

This does not mean, however, that EELS should be immediately abandoned for two very important reasons. In figure 7 we compare XEDS and EELS spectra measured in the same NiO specimen, where we have now expanded the horizontal scale to cover the same energy regime of 300-1000 eV for both data sets. The energy resolution available in EELS (~1 eV) is nearly 2 orders of magnitude better than that routinely achieved in XEDS (~100 eV). This is particularly important in complex alloy systems having multiple elements as the poor energy resolution in XEDS can preclude even qualitative light element analysis due to severe spectral overlap [Zaluzec et al. 1984]. In addition, the information content of the spectral profiles as we have discussed in the previous section is clearly markedly different.

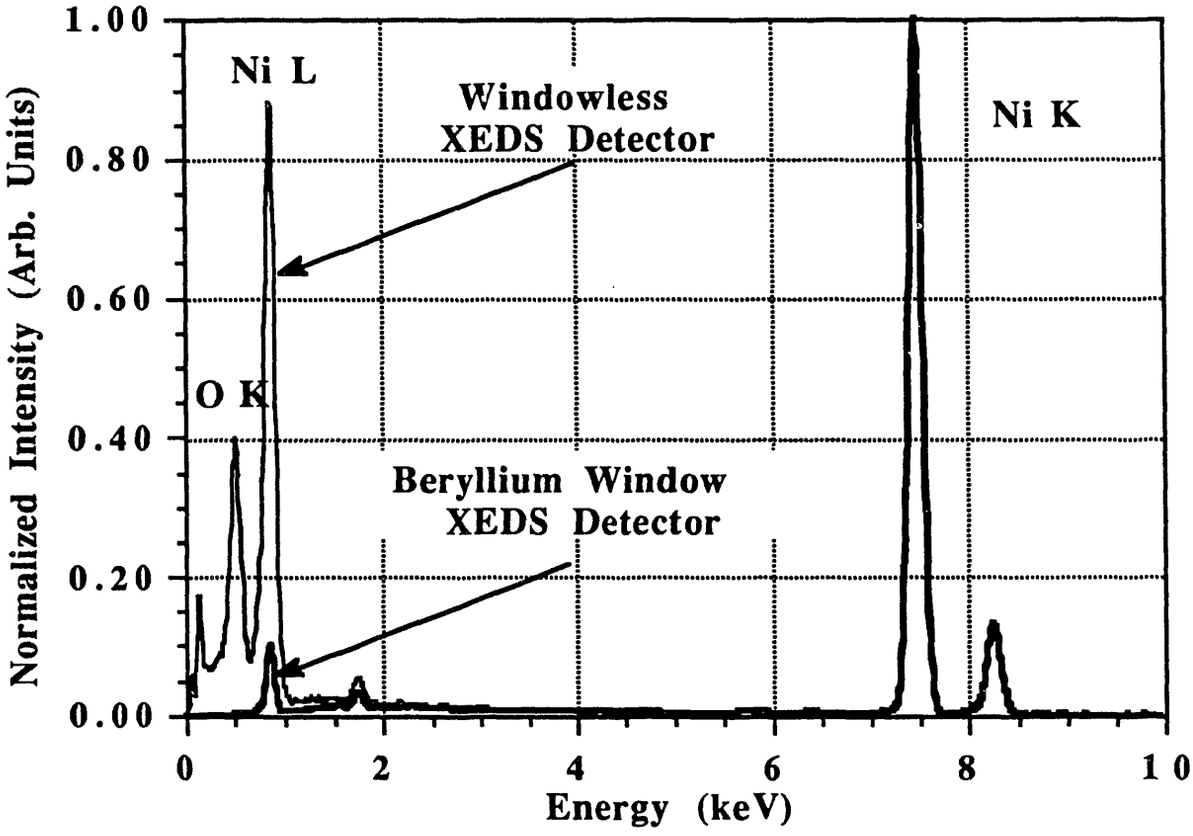

Figure 6. Comparison of XEDS emission using a windowless versus beryllium window detectors Note the enhanced detection efficiency below 1 keV for the WL detector. Both spectra are normalized to unity at the Ni Kα Line (7.48 keV)

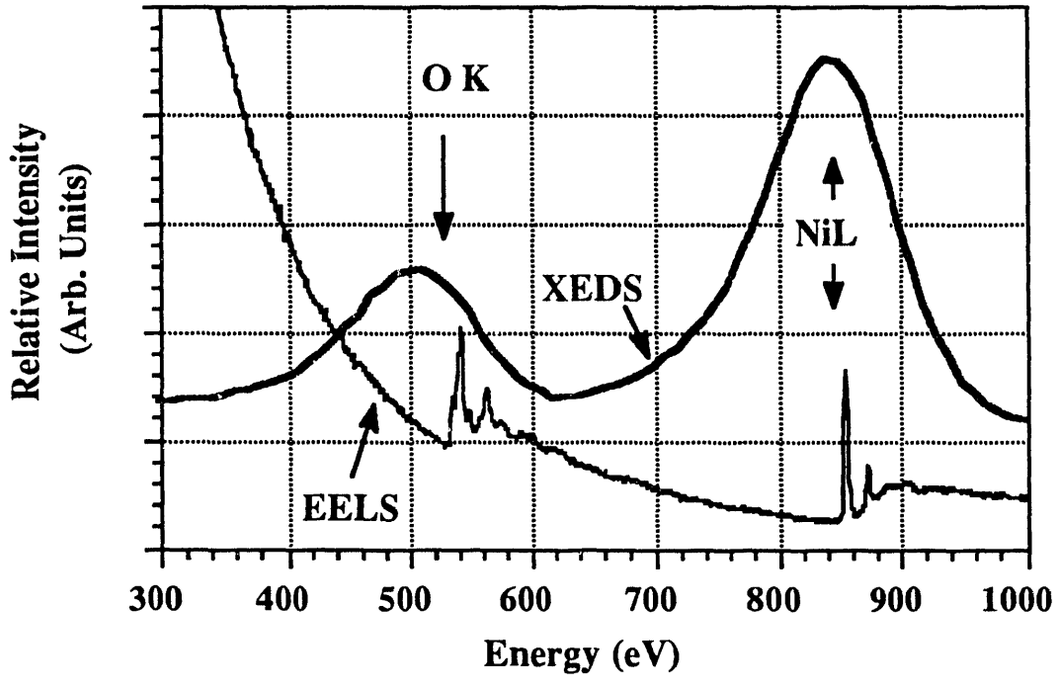

Figure 7. Comparison of WL XEDS Detector and EELS spectra taken from the same NiO specimen Note the enhanced spectral information in the EELS data. Vertical scale is arbitrary and chosen for clarity of presentation.

In chapter 3, EELS and XEDS were discussed in terms of detection limits and it was shown that EELS has greater sensitivity than XEDS for light element analysis (Z<20). It is important to note that these results generally apply only under conditions of very thin specimens ($t/\lambda \leq 1.0$). For thicker specimens multiple scattering can quickly result in a loss of the characteristic EELS signal so much so that EELS can become an impractical (although not impossible) technique. As an example of this, figure 8 compares EELS and XEDS K shell spectra from the thin (t/λ ~0.2) and thick (t/λ ~2) regions of a BN specimen. The loss in characteristic EELS edge signal which manifests itself by a decreasing in the Edge/Background Ratio is readily apparent. The BN x-ray data shown was recorded using a WL XEDS system which had marginal performance at Boron due to the presence of a low energy electronic noise peak, however, the detector shows reasonable sensitivity from carbon upwards in atomic number. Clearly one can see in this example that while EELS is becoming untenable, (the Boron signal is nearly undetectable above background and the Nitrogen is just measurable) characteristic x-ray detection of Nitrogen is still routine. The decrease in EELS sensitivity arises due to the rapid of increase in the EELS

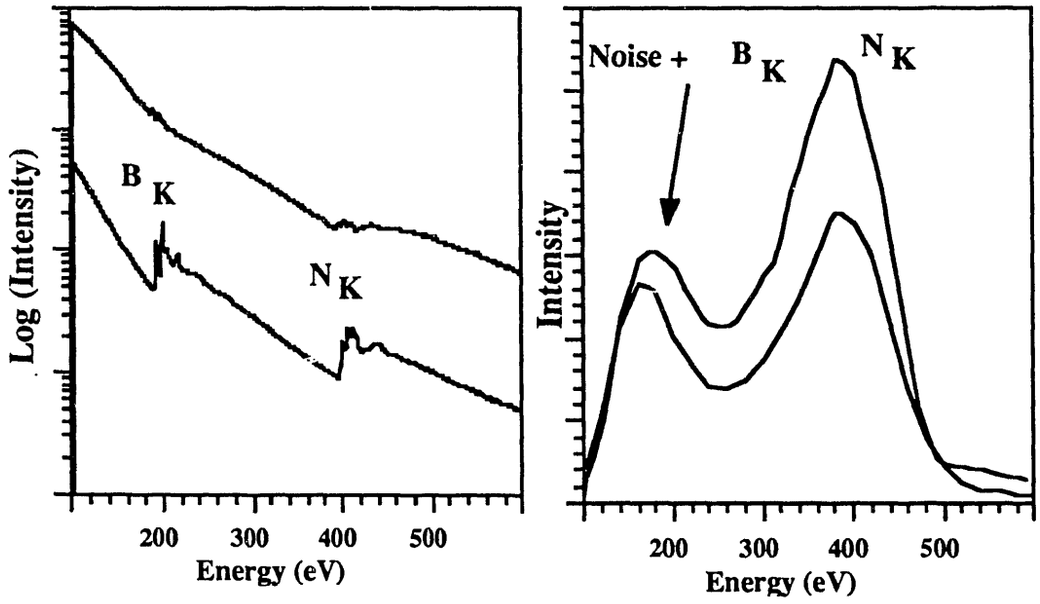

Figure 8. Illustration of the decrease in Edge/Background Ratio for the B K (~188 eV) and N K (~399eV) Shells in EELS compared to XEDS. In both data sets the upper profiles are from the thicker region of the BN specimen. The WL/XEDS detector has marginal Boron (Kα~183 eV) detection capabilities which are limited by a system noise peak at ~ 150 eV, the Nitrogen Kα line at ~390 eV is readily detected. Note the logarithmic scale for the EELS data.

background with thickness causing the characteristic edges to be less pronounced even though their net intensity is increasing. In contrast, the background in XEDS is generated by different processes than those involved in

EELS and hence for thicknesses where EELS is not usable ($t/\lambda \geq 2$), XEDS can still be routinely applied.

Another point to consider when assessing the merits of XEDS versus EELS for microanalysis rests in the quantification methodology. As outlined in Chapter 3 both techniques can employ relatively simple relationships equating experimental intensities to composition. These equations can be derived in the ***thin film approximation*** to have the general form:

$$\frac{I_A}{I_B} = \frac{\kappa_A \, \varepsilon_A \, C_A}{\kappa_B \, \varepsilon_B \, C_B} = k_{AB}^{-1} \frac{C_A}{C_B} \qquad \text{where } \kappa_A = \frac{\sigma_A \omega_A \Gamma_A}{W_A} \qquad (11\text{-}1)$$

Here $\sigma_A, \omega_A, \Gamma_A, W_A, \varepsilon_A, C_A$ and I_A are respectively the ionization cross-section, fluorescence yield, radiative partition function, atomic weight, detector efficiency, composition and measured signal intensity for the element A. The attractiveness of this formulation for quantitative analysis is that it states that the local composition of the specimen is directly proportional to the measured intensity of any two characteristic signals, multiplied by a series of proportionality constants and is independant of the local specimen thickness. For EELS the parameters ω, Γ, and ε are all unity, while for XEDS they vary in a systematic but well known manner with atomic number and energy of the measured signal [Zaluzec, 1979]. Unfortunately, the assumptions used in deriving this expression are valid only to finite thicknesses. The breakdown of this simple "thin-film" equation for quantitative analysis occurs at significantly smaller thicknesses for EELS than for XEDS. In the XEDS case, one ultimately becomes limited by x-ray absorption of one of the two signals within the specimen while in EELS multiple scattering dominates and limits one to $t/\lambda \leq 1$. The differences in thickness that this represents are not negligible and can easily exceed factors of ten. For example, EELS quantification in medium Z materials is limited to values less than 50-100 nm, while XEDS can in the same specimen might continue until in excess of 500 nm.

Another factor involved in quantification is the determination of σ, the partial ionization cross-section. These values are calculable (Chapter 3), however the requisite computations are significantly more involved than the total cross-section employed in XEDS where simple analytical expressions have been shown to be applicable. Accuracies in quantitative XEDS composition analysis can routinely reach the 2% level without difficulty, while the corresponding values for EELS are in the 10-20% regime. Lastly, the fabrication of composition standards which are not appreciably affected by thickness variation is significantly easier in XEDS than EELS mainly due to the fact that higher energy

(1-40 keV) transitions are used allowing thicker specimens to be employed. Thus the two methods should be considered complementary rather than exclusionary and the materials scientist should exploit both as appropriate.

Application of EELS to Materials Problems of Current Interest

Now that we have developed an overall picture of the relationship and limitations of analytical spectroscopies in the TEM/STEM, we shall now turn our discussion toward the application of EELS to studies of advanced materials. In the examples chosen next, EELS, was the analysis method of choice rather than any other spectroscopy. Keeping the preceding background information in mind, the motivations for this will become apparent during the course of the discussion.

Potential applications of EELS abound in materials science, the following studies were chosen from collaborative research on going in the Electron Microscopy Center at Argonne and illustrate the utilization of the technique to studies in High Tc superconductors (with A. Buxbaum - ANL/NU), multi-layer superlattices (with C. L. Foiles - MSU), amorphous magnetic materials (with T. I. Morrison -IIT), nuclear waste storage materials (with K. Smith-ANSTO) and hydrogen in metals (with B. W. Veal -ANL, and T. Schober- KFA Julich). In the examples herein, we will use the information in the low loss region to obtain valence electron densities from the plasmon losses, dielectric properties from the low loss spectral profiles, and use near-edge structures to identify important features of the materials studies. We will not consider simple quantification of the composition based upon edge integration in any of these examples as that has been covered elsewhere in this book.

Measurement of Valence Electron Densities:Studies of Hydrogen in Metals:

Metal-hydrogen systems have been of considerable interest in over the years because of their importance in various energy storage technologies and the phenomenon of hydrogen embrittlement. The detection of hydrogen by any other of the analytical methods outlined in the previous section is either possible, or not feasible. In contrast, the use of EELS to study hydrogen in metals was first reported by Coliex et al. in 1975, in that work and from Chapters 1 and 6 of this book we can show that using a simple free electron model the bulk plasmon energy (E_p) is given by the equation:

$$E_p = \hbar^2\omega_p = \sqrt{\eta \frac{\hbar^2 e^2}{m\varepsilon_o}} \qquad (11\text{-}2)$$

where e is the electron charge, m its mass, ε_o the vacuum dielectric constant, $\hbar$= Planck's constant/2π and η the valence electron density. From this relation we see that as the valence electron density changes so does the energy of the plasmon loss peak. Figure 9 shows partial EELS spectra from Mg, Ti, Zr and their hydrides, while Table 2 compares the results of calculations using free electron model (FEM) with experimental measurements [Colliex et al. (Sc, Y), 1975 and Zaluzec et al. (Mg, Ti, Zr, V, FeTi-,1982]. In general, the simple FEM provides a good estimate of E_p for most metals and their simple hydrides, however for the FeTi alloy system disagreement of ~ 14 % is obtained. This is not surprizing since in the higher atomic number transition metals the simple free electron model should not apply. This is due to the fact that higher Z materials contain a large number of d electrons which are more localized and, therefore, have a higher effective mass than s or d electrons of the lighter elements. This discrepancy can be accounted for if one reformulates the plasmon energy relation taking into account 2 sets of noninteracting electrons η_s and η_d with different effective masses m_s and m_d yielding the modified expression:

$$E_p = \hbar^2\omega_p = \sqrt{\frac{\hbar^2 e^2}{\varepsilon_o}\left(\frac{\eta_s}{m_s}+\frac{\eta_d}{m_d}\right)} \qquad (11\text{-}3)$$

Using the electron configuration of Fe as d^7s^1 and back calculating from the published values of E_p for pure Fe, one can obtain a value of m_d of ~1.9 m_e. Substituting this into the modified FEM equation we calculate for FeTi plasmon energy of 21.9, and for its two hydrides 21.8, and 21.5 as shown in the Table 2. This is now in good agreement with experiment.

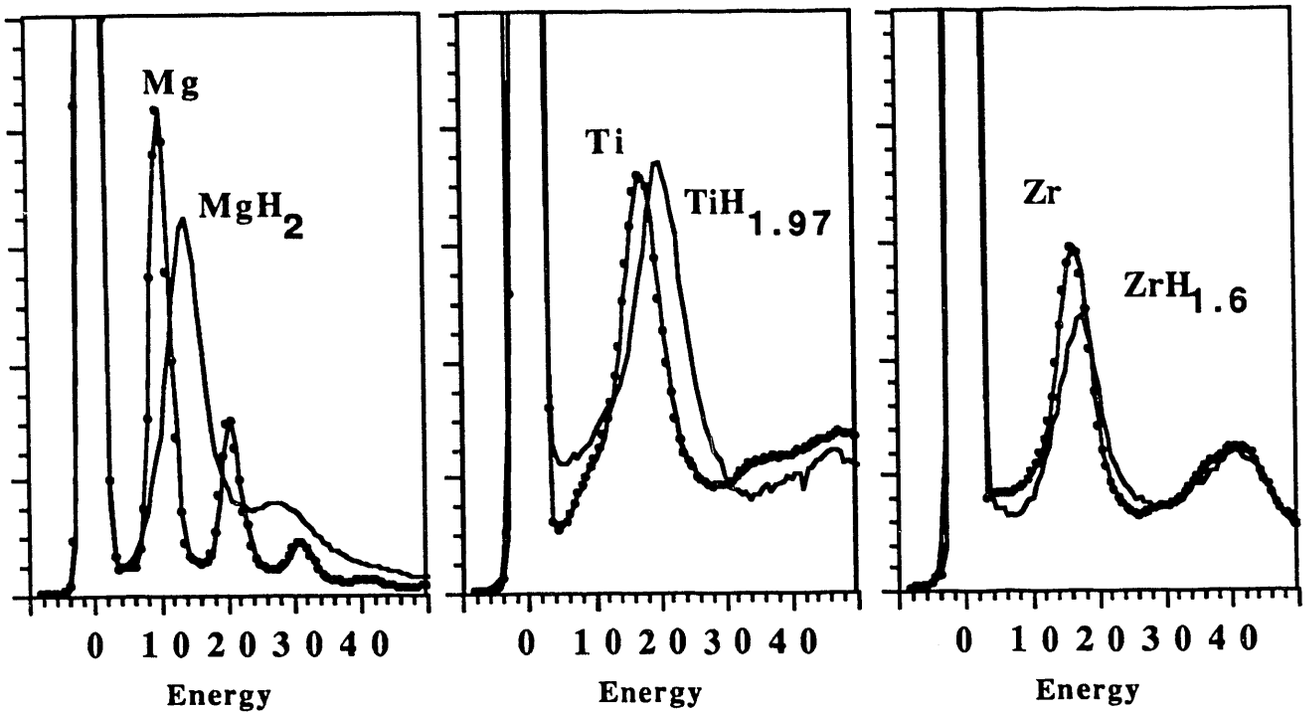

Figure 9. Experimental low loss profiles for Mg, Ti, Zr and their hydrides

If we plot the plasmon energy shift (ΔE_p) between the hydride and its metal divided by the relative hydrogen concentration (H/M) then we observe a systematic variation (in ΔE_p/H/M) as a function of periodic table group number. This is plotted in figure 10 and also documented in Table 3. Here the calculated values plotted on the graph refer to the simple FEM model, with the exception of the FeTi data which uses the both the FEM and modified FEM formulae described above. In this figure, we see that the most interesting materials relative to hydrogen in metals (Groups V and VI) show the smallest net shift. This effect simply reflects the negligible change in the valence electron density of these material as one adds hydrogen. For low Z transition metals the addition of hydrogen adds to the net electron density, while for higher Z metals with a large number of valence electrons the net effect becomes a reduction in the valence electron density, and hence not surprisingly one should expects a negative shift.

Table 3 Experimental and Calculated Plasmon Shifts in Selected Metal-Hydrogen Systems

Material	Expt. E_p (eV)	Calculated FEM	ΔE_p/H/M Expt.	ΔE_p/H/M FEM Calc.
Group II				
Mg	10.0 ± 0.5	10.90	2.1± 0.7	1.24
MgH_2	14.2± 0.5	13.38		
Group III				
Sc	14 ± 2 eV	12.87	1.6± 0.7	1.50
ScH_2	17.2 ± 0.5	15.87		
Y	12.5 ± 0.2	11.19	1.4 ± 0.7	1.41
YH_2	15.3 ± 0.5	14.0		
Group IV				
Ti	17.2 ± 0.5	17.69	1.4± 0.7	0.87
$TiH_{1.97}$	20.0 ± 0.5	19.4		
Zr	16.6± 0.5	15.37	0.9± 0.7	0.91
$ZrH_{1.6}$	18.1± 0.5	16.83		
Group V				
V	22.0 ± 0.5	22.29	0.0	0.3
$VH_{0.5}$	22.0 ± 0.5	22.44		
PseudoGroup VI				
FeTi	22.0 ± 0.5	25.04/21.9*		
FeTiH(β)	22.0 ± 0.5	24.65/21.8*	0.0	-0.84/-0.3*
$FeTiH_2$(γ)	22.0 ± 0.5	24.15/21.5*		

* Calculated using modified FEM with $m_s=m_e$ and $m_d=1.9\ m_e$

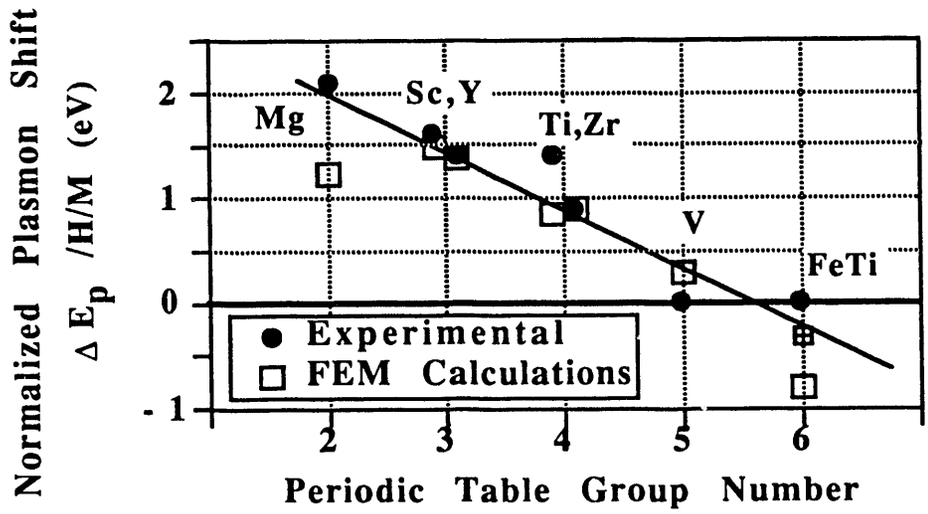

Figure 10. Normalized Plasmon shift from metal to hydride as a function of periodic table group number. For the FeTi Calculations both the FEM (empty square) and modified FEM (+ square) values are shown.

Dielectric Function Measurements:

In the preceding section we considered only one aspect of the low loss signal namely existence of the plasmon loss peak. One can reformulate the interaction and develop an expression which describes the interaction of electromagnetic radiation (the incident electron probe) with an absorbing medium in terms of conventional dielectric theory (Chapter 6). Thus as the fast electron looses energy in transmission through the specimen its interaction (i.e. the intensity of the measured loss spectrum I(E)) can be related to energy loss probability $P(E,\theta)$ which can be described using dielectric theory as :

$$I(E) = \int P(E,\theta)\, dE\, d\Omega \qquad (11\text{-}4)$$

where $d\Omega$ is the unit solid angle, t the specimen thickness, E_0 the electron kinetic

$$I(E) = \text{constant} * \frac{t}{E_0} \int \left(\frac{1}{\theta^2 + \theta_E^2}\right) * \mathrm{Im}\left(-\varepsilon^{-1}(E,q)\right) dE\, d\Omega \qquad (11\text{-}5)$$

energy, q the momentum vector, θ and θ_E the characteristic electron scattering angles and $\varepsilon = (\varepsilon_1 + i\,\varepsilon_2)$ is the dielectric function of the solid. By applying a Kramers-Kronig analysis (KKA) to the energy loss function ($\mathrm{Im}(\varepsilon(E,q)^{-1})$), the real part $\mathrm{Re}(\varepsilon^{-1})$ of ε can be computed from intensity measurements and then the real and imaginary parts (ε_1, ε_2) of the dielectric function determined. From these, one can then calculate the optical constants (refractive index N, absorption index K, and reflectivity R) for the material. The details of the mathematical reduction to obtain $\mathrm{Im}(\varepsilon(E,q)^{-1})$ from the experimental data I(E) as well as KKA are described in Chapter 6.

The advantages of electron loss measurements relative to more conventional optical measurements for dielectric property determinations are significant. First, being a transmission measurement, this technique is not dependent upon surface effects which can compromise or invalidate optical techniques. Second, energy loss data over an energy range of 500 eV or more are easily obtained. This range, about an order of magnitude greater than that of typical optical studies, is sufficient to uniquely determine the Kramers-Kronig

inversions that transform experimental data into real and imaginary parts of the dielectric function. Third, within the electron microscope it is a straightforward procedure to perform measurements as a function of momentum transfer or direction in the crystal lattice and thus orientation dependant studies may be easily performed. Fourth, electron energy loss measurements can be done on samples that range from microns to nanometers in size. Optical techniques typically require samples of millimeter dimensions. Each of the preceding advantages is particularly relevant to studies of the new High-T_C superconducting materials as well as multilayer and artificial superlattice specimens.

To begin, it is appropriate to compare as we have for the XPS and XEDS spectroscopies, the optical and energy loss experiments. For this we choose some recent work of Buxbaum (MS Thesis 1988 ANL/Northwestern University) in Copper. Figure 11 plots both the experimentally measured loss function ($\mathrm{Imag}(\varepsilon^{-1})$) for metallic copper obtained by both optical and EELS methods. As one can see the overall agreement in peak positions and magnitude between the two methods is very good considering the resolution of the EELS work was only ~ 2 eV while that of the optical work was < 1 eV. Figures 12 and 13 completes the analysis and presents a comparison of the complex dielectric constants ε_1 and ε_2 for both the optical and EELS procedures, it is a straightforward exercise to calculate macroscopic optical properties (N, K, R) of copper from this data.

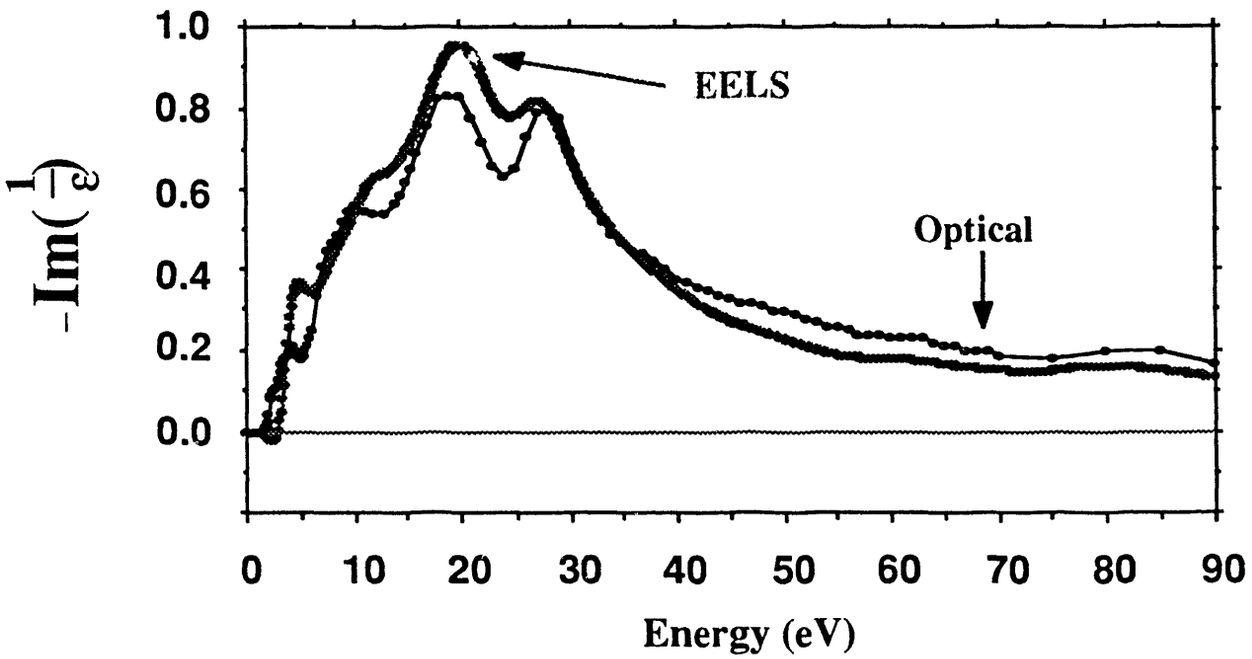

Figure 11. Comparison of the loss function of Cu obtained by EELS (Buxbaum-1988) and Optical Methods (Weaver et al.. 1981).

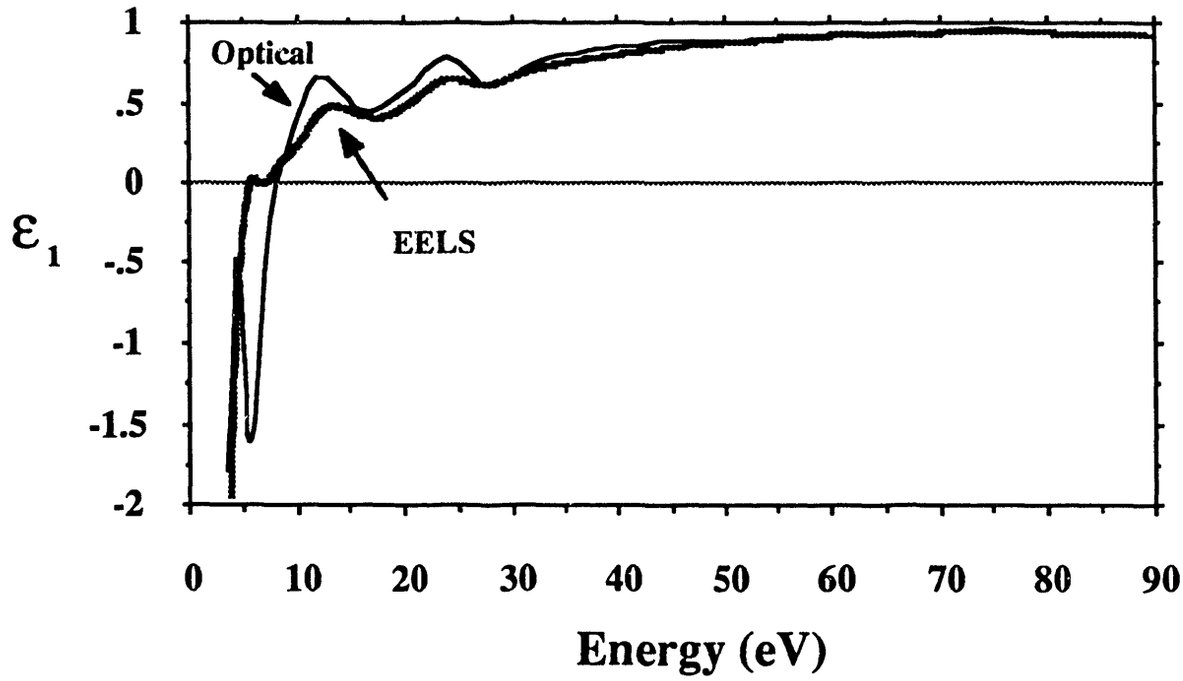

Figure 12. Comparison of Real Part of the complex dielectric constant for Cu obtained by EELS (Buxbaum-1988) and Optical Methods (Weaver et al.. 1981).

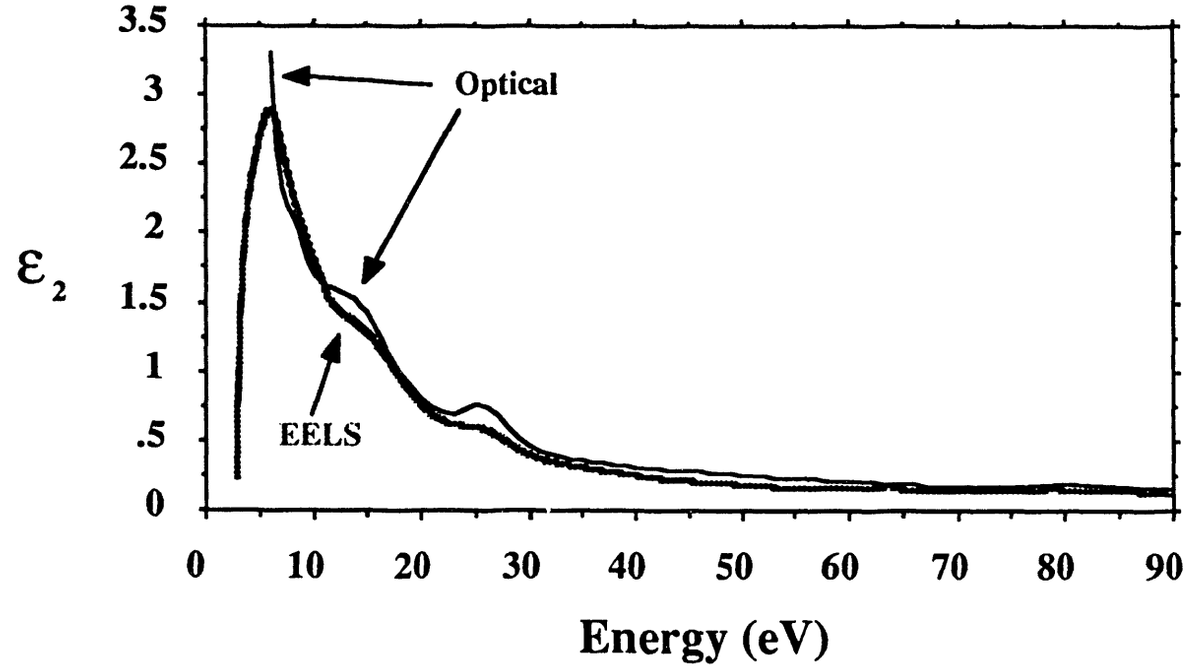

Figure 13. Comparison of Imaginary Part of the complex dielectric constant for Cu obtained by EELS (Buxbaum-1988) and Optical methods(Weaver et al.. 1981).

The major discrepancies between the optical and EELS methods shown in the data of figures 11-13, occurs in the region below ~ 5eV. As pointed out in Chapter 6, this is the region where the finite width of the Zero Loss peak

overlaps the inelastic scattering the most and as a consequence, obscures or distorts the experimental data. In this work the FWHM of the Zero Loss peak was ~ 2 eV, modern field emission gun systems can reduce this value to ~ 0.3 eV or better. Such improvements will clearly improve the results. The more closely the materials studied approximate a free electron solid (i.e. low Z materials and/or semiconductors) the better the results become [Buxbaum, 1988]. In such systems interband transitions are well separated from the plasmon oscillation region, in contrast, to the transition metals where strong effects in the 0-3 eV regime are known to exist.

Artificial Metallic Superlattices

Turning from simple pure element applications the utilization of EELS in studies of artificial superlattices allows us to use the electron microscope as a probe of both the atomic as well as electronic structure of these novel new materials. Composed of ordered bilayer arrays of metallic elements these compounds form a new class materials with corresponding unique properties (Falco and Schuller, 1985). By varying both metals used in the bilayer unit and/or the layer thickness the scientist has a means for controllably altering the properties of the systems and by extension the behavior of ε. Relatively simple metallic multilayers with sharp and partially coherent interfaces of Mo/V are used in this example each having symmetric bilayers spacing of from 10 to 40 monolayers. Each pure element has a BCC structure with their lattice parameters differ by ~ 3.9%. As the metallic bilayer superlattice spacing is decreased below about 30 monolayers, the onset of a structural transformation results in effects which are not simple linear combinations of pure element properties. These changes corresponds to the formation of a single strained layer BCC superlattice, and mirrors changes in the superconducting temperature. This should not be surprising since as the multilayer wavelength is decreased the interactions of the individual layers becomes more pronounced. As one would expect EELS measurements reflect a transition between between the noninteracting elemental layers and the formation of the long period superlattice. Figure 14 shows the experimental changes in ε_1 for for nominal 40ML/40ML (squares), 30ML/30ML (circles) and 20ML/20ML (triangles) Mo/V superlattice samples, while the solid line is calculated based upon known optical properties of the pure metals.

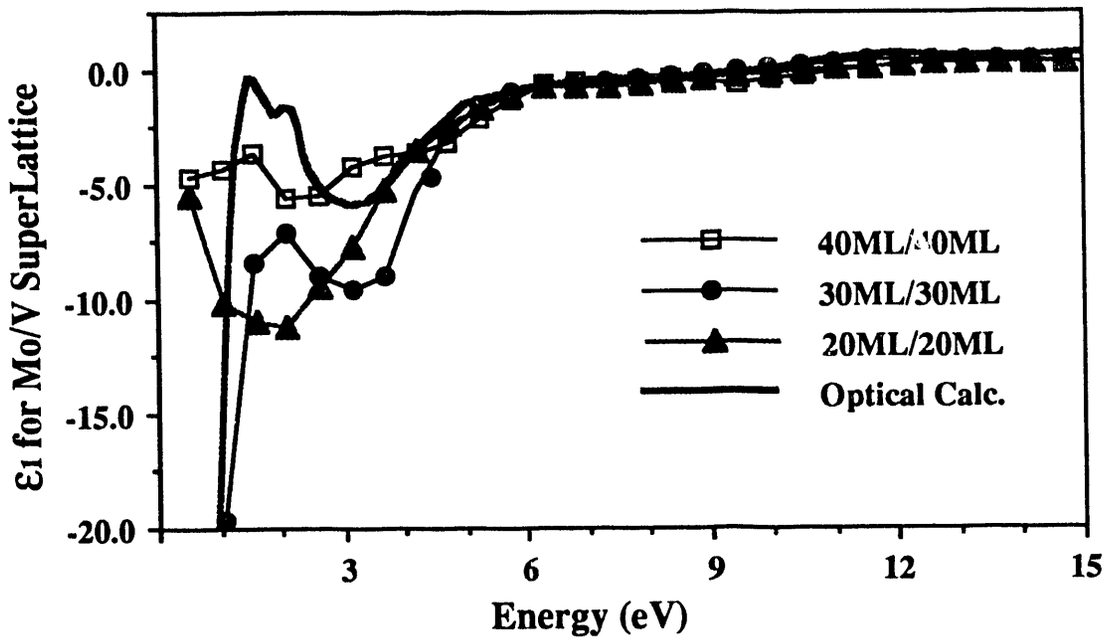

Figure 14.) Real part of the dielectric function (ε_1) compared to optical calculations for various thicknesses of Mo/V superlattices.

As the bilayer thickness decreases from 40/40 through 20/20 we see a increasing shift in the shape of ε_1 which deviates from the simple linear combination shown in the optical calculations. These differences correlate with the onset of a structural transformation, i.e. the formation of a strained layer superlattice, in this thickness range, which has also been verified by electron diffraction.

High T_c Superconductors

Figures 15 and 16 illustrates the results of room temperature measurements of the anisotropic loss functions and dielectric constants ε_1 and ε_2 for $Y_1Ba_2Cu_3O_{7-\delta}$ measured both parallel and perpendicular to the C axis of the High-T_C superconductor. Here again the ability to perform localized studies becomes an important part of the application in EELS. In this case the specimen size (< 0.5 mm) and grain size (~1 μm) was such that conventional optical methods cannot be practically employed. In addition, the fact that the analytical electron microscope has specimen double tilt stages which permit control of local orientation allows one to more fully characterize the orientation dependant properties of submicron single crystal volumes. These results demonstrate not only the feasibility of low loss measurements in the Y-Ba-Cu-O system but also the possibility of exploring the anisotropy which exists in non-cubic systems.

The energy resolution of present instrumentation used for this work is limited by the kinetic spread of the electron beam, which for these measurement was ~2 eV. This resolution can be improved slightly by mathematical deconvolution of the instrument function, however, significant progress in this area rests primarily with better instrumentation employing field emission sources. In superconducting materials, electronic states exist which the range from a few tens of meV to roughly 40 eV and this clearly presents a limitation. Fortunately, the use of Kramers-Kronig inversions of energy loss data means that the dielectric function is not determined completely by direct measurements and thus valuable studies using the present instrumentation can still be carried out.

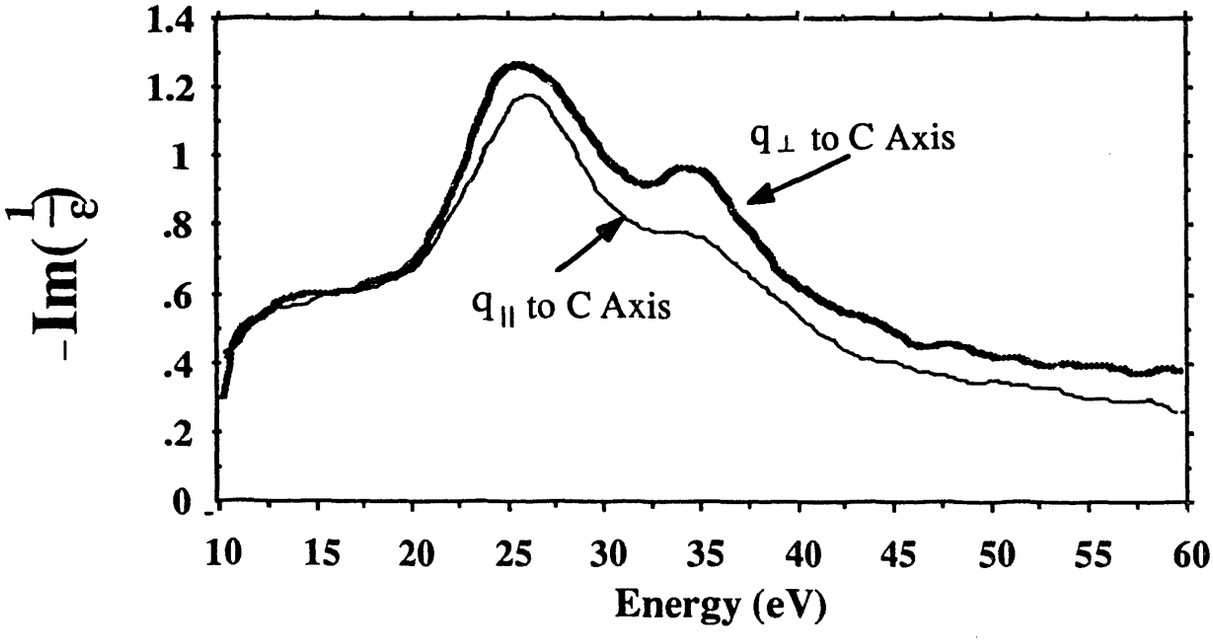

Figure 15. The loss function for $YBa_2Cu_3O_{7-\delta}$ for polarization parallel and perpendicular to the C-axis.

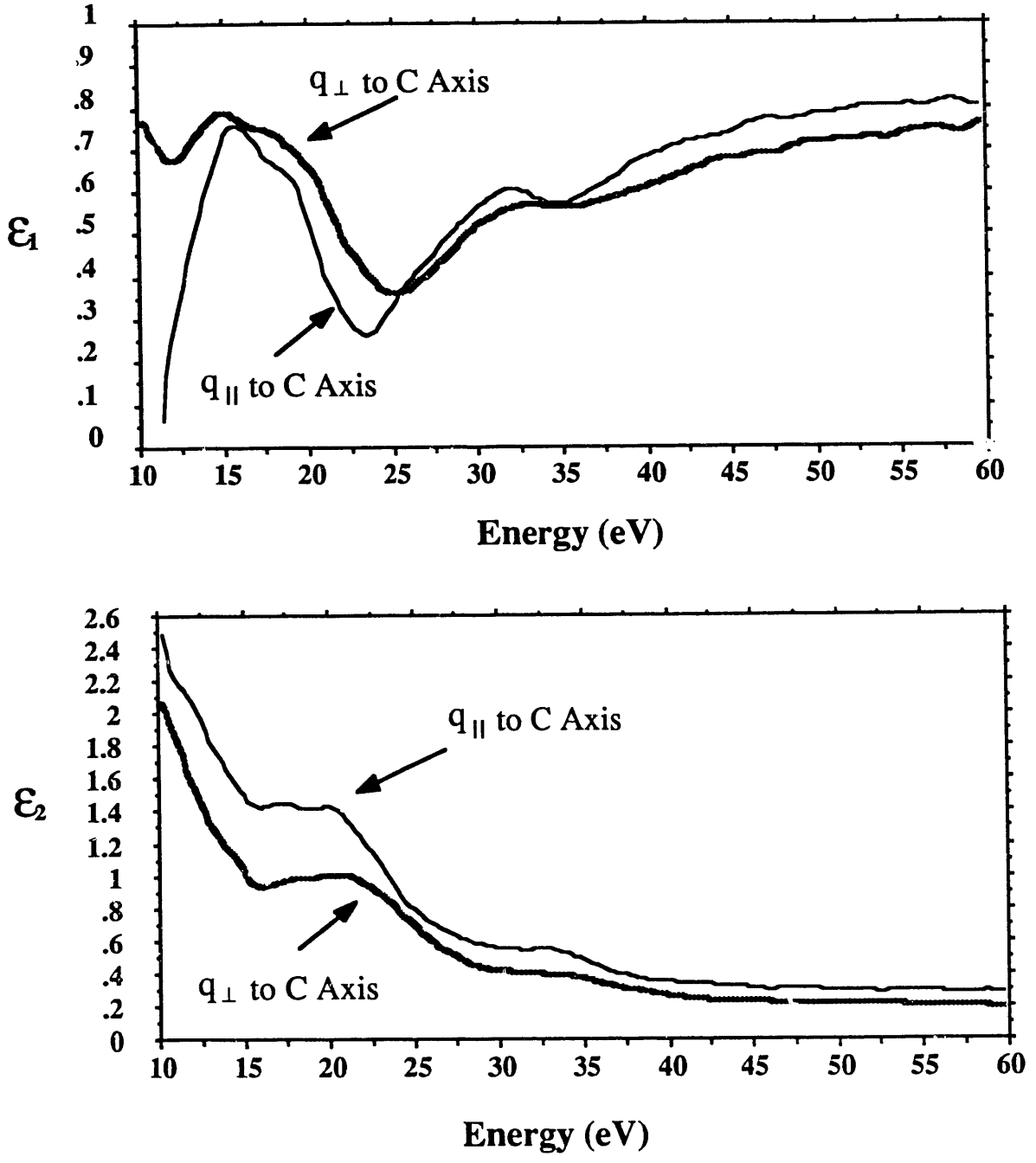

Figure 16. The real and imaginary parts of the dielectric function of $Y_1Ba_2Cu_3O_{7-\delta}$ measured for polarization vector parallel and perpendicular to the C-axis .

Core Loss Spectroscopy:

As we discussed earlier in this chapter, there is a wealth of information in core loss spectra beyond the simple composition measurements, which originally drove much of the development work in EELS. In this section we shall select examples which illustrate the application of EELS measurements to inner shell losses.

Valence Studies in Ti-based Ceramics

Chemical shift studies are well known in photoelectron spectroscopy and although EELS measures different transitions, similar effects are also observed (Leapman et al., 1982). For example in oxidation of metallic elements, charge is transferred from the metal to the oxide. Since the metal atom is giving up some of it's electrons, it's net nuclear potential becomes more attractive and hence the energy levels of the shift downward. This results in corresponding change in energy of the metallic species edge onset position. These "chemical" or alloying effects are not only restricted to absolute energies as near edge fine structure can also be affected. Figure 17 shows partial spectra from two different Titanium oxides: Perovskite ($CaTiO_3$) and Barium-Hollandite ($BaAl_2Ti_6O_{16}$), both important phases in SYNROC a candidate nuclear waste storage material. From these spectra we can immediately infer that the valence state of Ti in the Hollandite is less than that of Perovskite (+4) since it is shifted downward in energy by ~ 1 eV. Furthermore, in addition to the spin orbit splitting which is manifested by the L_3 and L_2 edges (split about 5 eV) we can observe a secondary splitting in the Ti L edges in the Perovskite which is not present in the Hollandite. This second splitting of about 2.5 eV is likely due to the octahedral coordination of the Ti atoms with the O (in the TiO_2 structure) causing degenerate molecular levels.

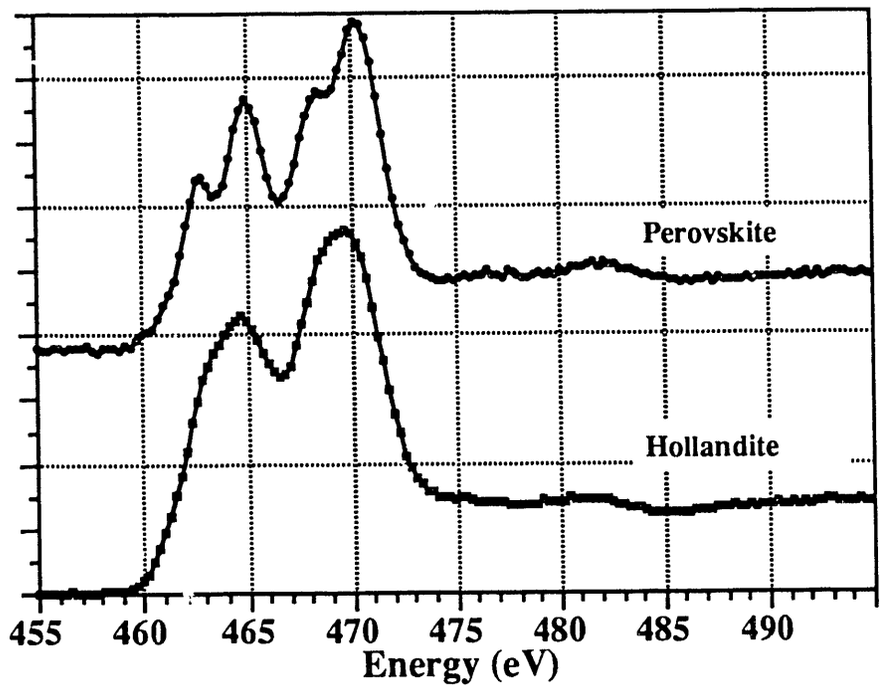

Figure 16. Ti L shell spectra from Perovskite and Hollandite phases in SYNROC.

Amorpnous Magnetic Materials

Magnetism in amorphous binary alloys of the type M_xA_{1-x}, where M is a magnetic transition metal (Fe, Co, Ni) and A a metalloid (B, Si, Ge, Sn) has been a topic of study for over twenty years. These systems have the interesting property that the magnetic moment per magnetic atom decreases monotonically with increasing metalloid content and since they are amorphous this change must be due to short range order effects. The explanations for the phenomenon have been attributed to charge transfer from the *3d-band* of the magnetic species or due to band broadening by hybridization of orbital of the nonmagnetic species. Although these systems have been studied extensively by resistivity, Mossbauer and XPS the results have not been definitive. EELS studies of the L_3 and L_2 edges, however, provide a direct and simple solution to the determination of the number of *d-band* holes in transition metals. Here the sum of the amplitudes of the L_3 and L_2 edges is directly proportional to the number of holes in the band, since these spectral features are dominated by $2p_{3/2}$-> $nd_{5/2}$ and $2p_{1/2}$-> $nd_{3/2}$ transitions respectively (Morrison et al. 1985, Pearson et al. 1988). The ratio of the number of holes in the 5/2 to 3/2 states can be shown to be directly related to the integrated amplitudes of the L_3 and L_2 edges by the formulae:

$$\frac{h_{5/2}}{h_{3/2}} = \frac{1}{6}\left[\frac{5}{2}\frac{I_{L_3}E_{L_3}}{I_{L_2}E_{L_2}} - 1 \right] \qquad (11\text{-}6)$$

where I_L is the Lth shell edge amplitude and $E_L = \left[\hbar\omega_L\right]$ its energy. The edge amplitudes are obtained by fitting Lorenzian curves to the background subtracted edge profiles and then normalizing to the L shell cross section. Figure 17 show a sequence of Fe L shell spectra for the Fe_xGe_{1-x} system with increasing Fe composition. From this data one can determine both the total number of hole in the d-band as well as the ratio of the $d_{5/2}$ and $d_{3/2}$ holes. These results are given in table 3 and plotted in figure 18. A careful inspection of these spectra shows that the ratio of the amplitudes of the peaks change with composition. This implies that the holes are redistributing themselves between the states of 5/2 and 3/2 symmetries. On the other hand, the total number of holes in the *d-band* is remaining relatively constant across the composition range although the magnetic moment changes from roughly 2 to nearly zero Bohr magnetons. Since the iron d-band is more than half full, the redistribution of holes must correspond to a change in spin-pairing which would explain the dramatic change in moment.

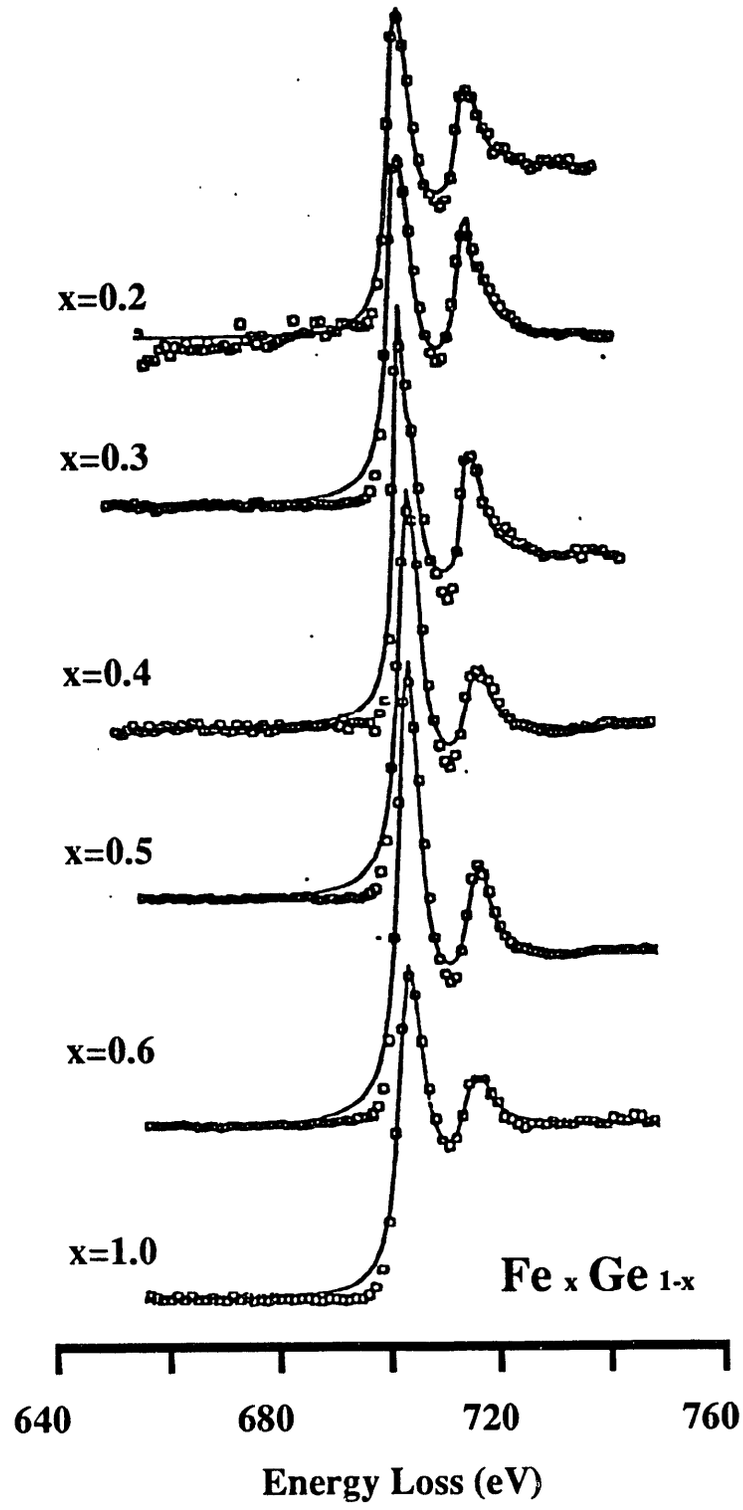

Figure 17. Experimental L_{32} edge for Fe_xGe_{1-x} normalized to the total number of Fe atoms. Open square are experimental data; solid line is the best fit to the data.

Table 3
Variation in *d-band* occupancy with composition in Fe_xGe_{1-x}

Composition	$h_{Total}/h_{Total}(Fe)$	Ratio $h_{5/2}/h_{3/2}$
1.0	1.0	0.68
0.6	1.3	0.69
0.5	1.1	0.72
0.4	1.1	0.4
0.3	1.3	0.29
0.2	1.0	0.45

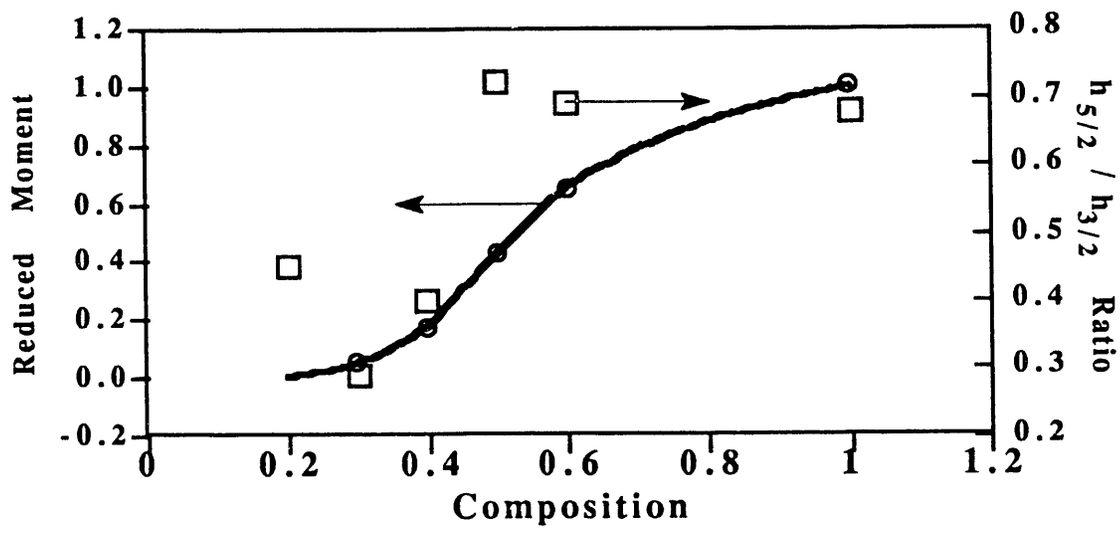

Figure 18 comparison of variation in reduced magnetic moment (open circles) to ratio of $d_{5/2}$ and $d_{3/2}$ holes (squares) as a function of composition in Fe_xGe_{1-x}.

High T_c Superconductors

High T_c superconductors are, to understate the obvious, somewhat interesting materials. Slight changes in oxygen stoichiometry can cause huge changes in their properties taking the solid from metallic to insulating states and back again. Although XEDS is a useful tool in investigating gross composition changes, in these materials it does not have sufficient sensitivity to provide detailed information which allows one to differentiate between good and bad systems. Consider the $Y_1Ba_2Cu_3O_{7-\delta}$ case for example. The difference between a

High T_c Superconductor having an oxygen concentration of ~6.9 with a T_c near 92 K, a Medium T_c superconductor at oxygen ~ 6.6 with a T_c near 60 K and the insulator with oxygen ~ 6.4 corresponds to an overall change in the oxygen concentration from 53.5 to 51.6 at%. The ability to measure quantitatively absolute changes at this level (or better) taxes or in most cases exceeds the capabilities of XEDS in the analytical electron microscope. XEDS spectra of High T_c's (figure 19) simply do not have sufficient resolution or sensitivity to be able to routinely reach this level of differentiation. Subtle changes in the oxygen signal are simply lost due to the poor resolution of the detector.

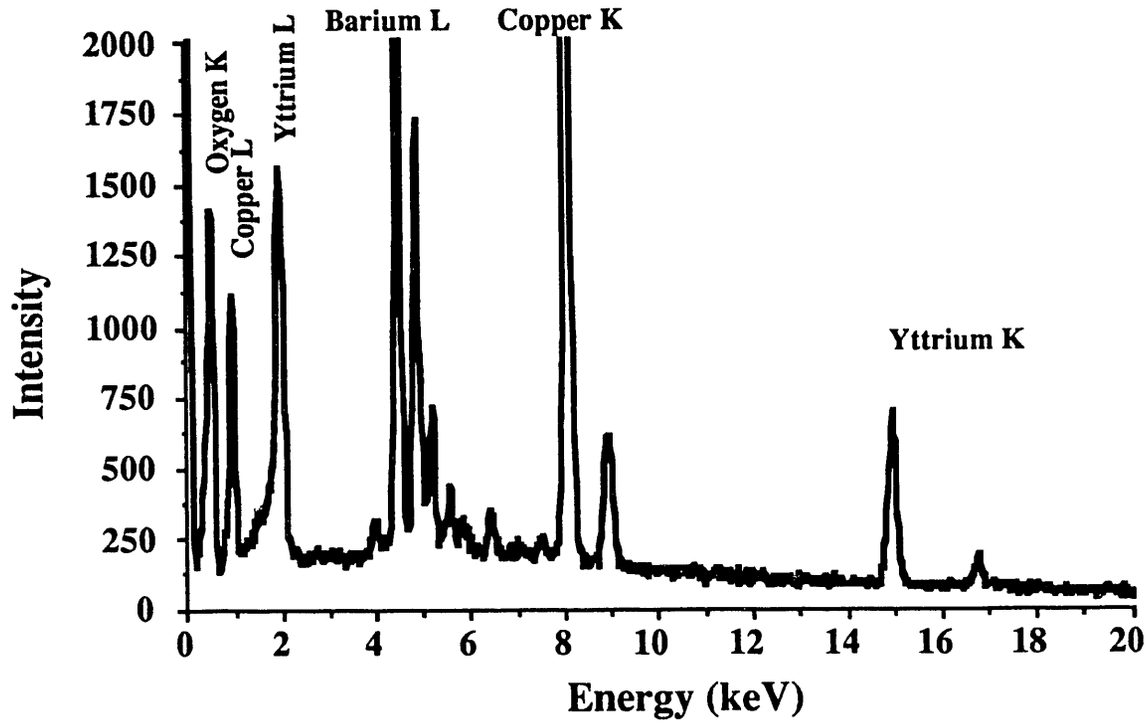

Figure 19. UTW XEDS spectra from $Y_1Ba_2Cu_3O_{7-\delta}$

EELS, however, does not suffer the same limitations as we have seen earlier in this chapter. Figure 20, for example, shows the small yet distinct change in the Oxygen K shell profile in the $Bi_2Sr_2Ca_{n-1}Cu_nO_x$ system (T_c~105 K) between a superconducting and non-superconducting specimen. The change in the Near Edge Structure (NES) directly correlates with the loss in superconductivity and has been reported in LaSrCuO (Nucker et al. 1987) and the YBaCuO systems as well (Batson and Chisholm, Sabatini et al., 1988). This peak can be interpreted as the existence of "hole" states just above the Fermi level and it is appropriate to note that the loss of superconductivity correlates with the disappearance of this state. Whether it has direct bearing on superconductivity is a separate issue which needs further investigation. This O K shell NES is also orientation dependent. In figure 21, we can see that when the momentum transfer from the

incident probe is perpendicular to the *c*-axis (i.e. the scattering is confined to the *ab* plane) then the intensity of the pre-edge peak increases and decreases perpendicular to this plane. The O K shell edge signal corresponds to *s->p* transitions and since the *1s* state is spherically symmetric this orientation dependance can be used to probe the orientation of this hole state. Since the intensity decreases when the scattering contains the c-axis this implies that if the states exist they must be partially filled, thus from this simple orientation study one can conclude that the final "hole" states must have $p_{x,y}$ symmetry.

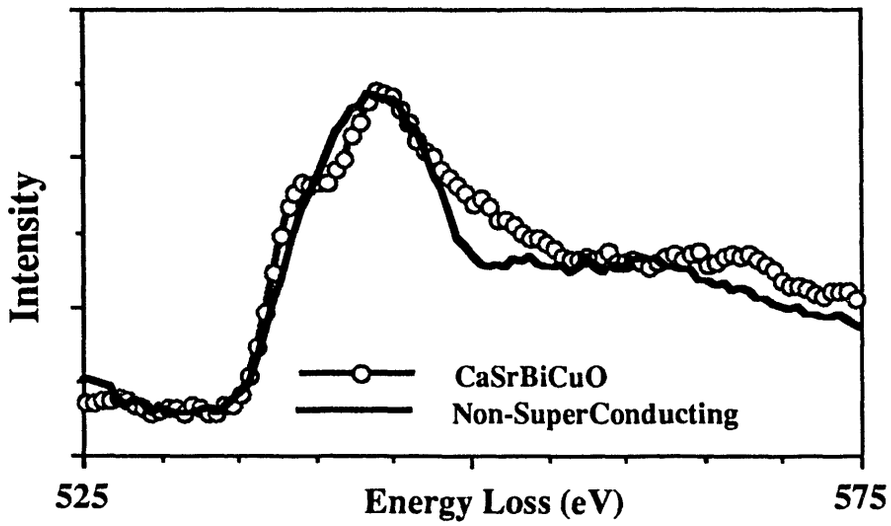

Figure 20. Oxygen K Shell in superconducting and non-superconducting specimens in the $Bi_2Sr_2Ca_{n-1}Cu_nO_x$ system. Note the disappearance of the pre-edge peak in the non-superconducting specimen.

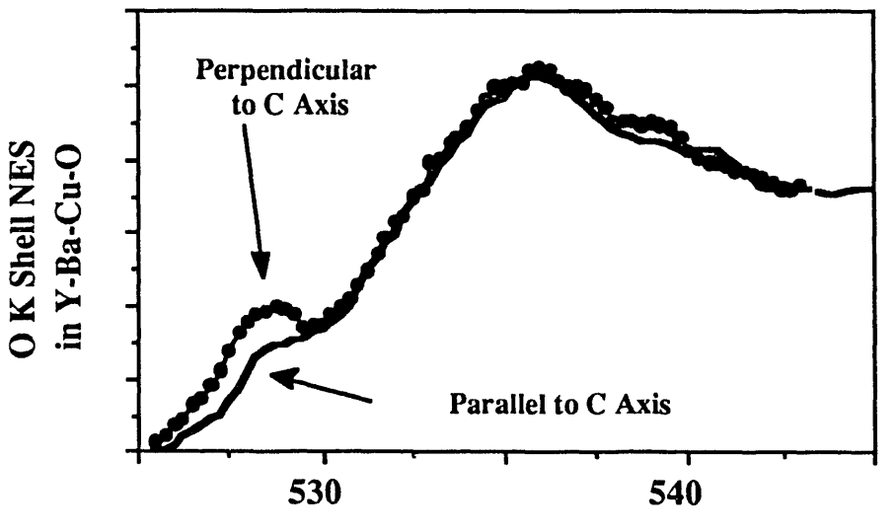

Figure 21. Orientation dependance of the O K shell in $Y_1Ba_2Cu_3O_{7-\delta}$. The intensity variation of the pre-edge peak indicates that the hole state just above the Fermi level has $p_{x,y}$ symmetry. Parallel and perpendicular here refer to the momentum transfer directions which are by conservation perpendicular to the incident beam directions.

There are a great deal of other edges available for study in High T_c materials in the range of 0-1000 eV. The higher Z elements (Y, Ba, Bi, Sr, Ca, and La) which form the building blocks of the ABO_3 perovskite structure, common to all the High T_c's, are detectable as M and N shell edges of varying prominence. However, besides the oxygen edge the only other elemental candidate which seems to have direct influence on the superconduction properties is copper through its ordered substructure of chains and planes [Veal and Chan 1989]. If we examine the Cu edges then we see that two candidates are available to us, the M_{32} at ~ 70 eV and the L_{32} at ~930 eV. The low energy Cu M shell is not amiable to rigorous study at this time, due in part to the high background and N shell edges nearby from the higher Z elements. The copper L shell is marginally better, generally riding on the tail of the M_{54} edges of Y, Ba or La(depending on the alloy). Simple background stripping (Chapter 3) is generally sufficient to extract the Cu L edge profiles without major effort, although the edges are relatively small. In figure 22, we compare the L shell profile of Cu in $Y_1Ba_2Cu_3O_{7-\delta}$ with that of Cu metal (valence =0), Cu_2O (valence =+1), and CuO (valence=+2). In $Y_1Ba_2Cu_3O_{7-\delta}$,, Cu_2O, and CuO

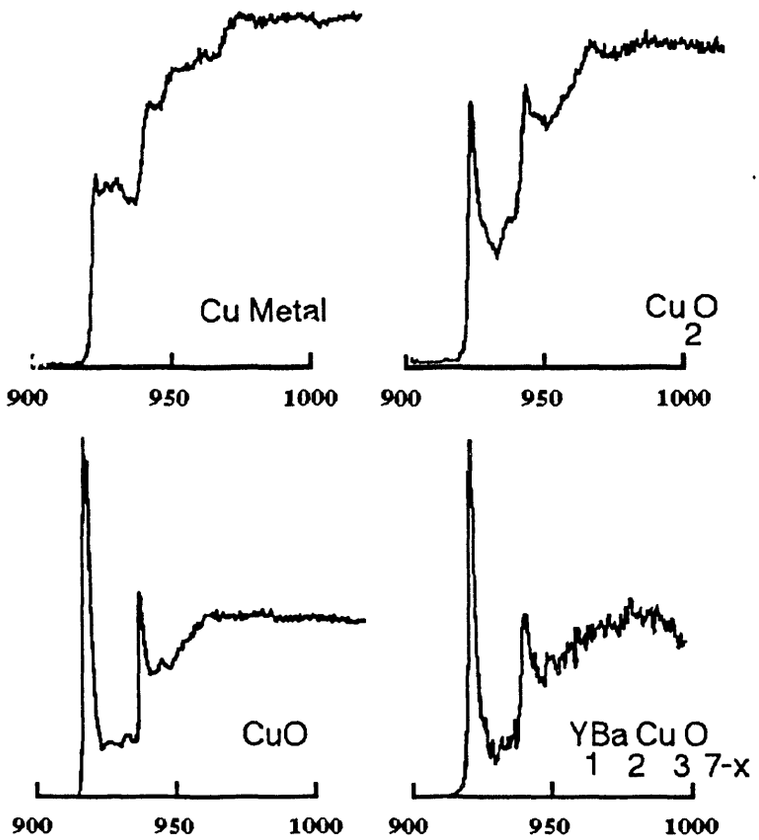

Figure 22. L shell spectra from Cu metal, Cu_2O, CuO and $Y_1Ba_2Cu_3O_{7-\delta}$. The change in the relative L shell profiles reflects the changing *d-band* hole population and valence state of the four materials.

electron transfer from the Cu *d-band* to the Oxygen atoms has occurred. This in effect shifts the Fermi level and creates unoccupied states which are now probed

by EELS. In all cases studied, for $Y_1Ba_2Cu_3O_{7-\delta}$ the white lines at the onset of Cu are present and are of at least the same relative intensity of CuO, rather than Cu_2O. This implies, that the average valence state of Cu in the $Y_1Ba_2Cu_3O_{7-\delta}$ is at least +2 or higher. Unlike the O K shell no significant orientation dependence of the L shell intensities has been observed.

Summary

In this chapter we have briefly compared the information in the different electron and x-ray spectroscopies generally available in materials science. The two most prevalent in conjunction with the analytical electron microscope: XEDS and EELS, were contrasted and compared and the limitations of each addressed. XEDS is primarily used for elemental composition determinations in the AEM, while EELS can be additionally employed to determine the electronic properties of solids. Although EELS is ultimately limited by multiple scattering effects due to specimen thickness there are a class of materials problems which can be uniquely addressed and solved using this methodology. By means of example, EELS was used to elucidate the nature of several advanced materials issues which involve the electronic structure of materials and require higher spatial resolution than is afforded by the more conventional spectroscopic techniques.

The future for EELS in materials research is quite promising. The early efforts of the analytical microscopists which sought to exploit the light element detection capabilities of this technique have now expanded to applications in electronic structure analysis. The development of new analytical instrumentation having high brightness and low energy spread field emission electron sources as well as more efficient parallel detection systems will result in the rapid growth of the application of this analysis method to more and more complex problems in materials research and at an every decreasing spatial scale. Once regarded as a tool for simple light element composition measurements EELS has established it complementary role in the list of quantitative analysis techniques for state-of-the-art materials research.

References

Batson P. and Chisholm M., JEMT, 8, No. 3 PGE 311 (1988)

Buxbaum A.H. "Methodology for the study of optical properties of solids by EELS with an application to YBaCuO. M.S. Thesis Northwestern University - Evanston Ill. 1988

Colliex C. And Trebbia P. In"Developments in Electron Microscopy and Microanalysis" p 123 (1975) Academic Press

Falco C.M. and Schuller I.K. in "Synthetic Modulated Structures", Academic Press Orlando Fl, (1985)

Leapman R.D. , Grunes, L.A., Fejes, P.L. Phys Rev. B26, 614 (1982)

Morrison T.I. , Brodsky M.B. and Zaluzec N.J., Phys. Rev. B. 32, 5, p 3107 (1985)

Nucker N., Fink J. Renker. B. Ewert D., Politis C. Weijs P. and Fuggle J. . Z. Phys. B67:9-14, (1987)

Pearson D.H., Fultz B. and Ahn C.C. Appl. Phys. Lett. 53 (15) 1988 page 1405

Sabatini R., Heald S., Suenaga M, Moodenbvaugh A., Jones R. , JEMT, 8, No. 3, 1988 page 307

Veal B. and Chan S.K. Sintering, 1990 Proceeding of the VII World Round Table Conference on Sintering, Herceg-Novi, Yugoslavia, Sept. 1989

Zaluzec N.J. Proc. of the Xiith Int. Congress for EM, Seattle-1990 page 130, San Francisco Press. 1990

Zaluzec N.J., McConville R., and Sandborg A. , Analytical Electron Microscopy 1984, San Francisco Press.page 348 Ed. Williams, and Joy.

Zaluzec. N.J., Schober T., Veal B.W. in Analytical Electron Microscopy-1982 Proc. of Workshop at Vail Colorado, San Francisco Press. pg. 191

Zaluzec N.J. in "Introduction to Analytical Electron Microscopy" Chapter 4, pg. 121 Plenum Press, 1979, Ed. Hren, Goldstein, Joy

Index of Terms used in the Chapter:

XEDS, WDS, CL, EELS, EXELFS, ELNES, AES, PES, XAS, EXAFS, XANES, XPS,UPS, XRF
Inner Shell, Valence Band, Conduction Band, Density of States, Plasmons,
Dielectric Properties, Chemical Shifts,
Thin films, Quantitative Analysis,
Superconductors, Superlattices, Hydrogen in Metals, Transition Metals,
Amorphous materials, Magnetic Materials.

END

DATE FILMED

01/02/92